

See discussions, stats, and author profiles for this publication at: <https://www.researchgate.net/publication/231646596>

Electronic Structure of TiO₂ Surfaces and Effect of Molecular Adsorbates Using Different DFT Implementations

ARTICLE *in* THE JOURNAL OF PHYSICAL CHEMISTRY C · DECEMBER 2010

Impact Factor: 4.77 · DOI: 10.1021/jp109756g

CITATIONS

52

READS

178

3 AUTHORS, INCLUDING:



Natalia Martsinovich

The University of Sheffield

60 PUBLICATIONS 875 CITATIONS

[SEE PROFILE](#)

Electronic Structure of TiO_2 Surfaces and Effect of Molecular Adsorbates Using Different DFT Implementations

Natalia Martsinovich,* Daniel R. Jones, and Alessandro Troisi

Department of Chemistry and Centre for Scientific Computing, Warwick University, Coventry, United Kingdom

Received: October 11, 2010; Revised Manuscript Received: November 12, 2010

We model TiO_2 rutile (110) and anatase (101) surfaces and investigate the effect of adsorption of benzoic acid on the electronic structure of these systems. The surface–adsorbate electronic structure determines the rates of electron-transfer processes, which are important for dye-sensitized solar cells, in particular. We use density functional theory (DFT) and test the accuracy and efficiency of several DFT implementations (plane waves vs localized basis sets, all-electron vs pseudopotential calculations) as applied to the TiO_2 –adsorbate system. We explore the variation in the band gap, surface energies, and benzoic acid adsorption energies as a function of slab thickness. Our results show that a two-layer slab is sufficient to model the adsorption of benzoic acid on anatase, whereas for rutile, convergence is much more slow and not yet achieved in five-layer slabs. The effect of the adsorbate on the electronic structure is small in the case of anatase, but noticeable for rutile, where adsorbate states appear near the valence band edge, and TiO_2 states near the conduction band edge are shifted upward. The TiO_2 surface layers make a small contribution to the density of states near the conduction band edge, but a prominent contribution deeper in the conduction band, at energies where electron injection from sensitizing chromophores is most likely to occur.

1. Introduction

The very large number of applications of TiO_2 in materials science is, almost without exception, ultimately a result of the facile electron-transfer processes that occur at the interface between the semiconductor and adsorbed molecules. When photoexcited, TiO_2 is a good electron and hole donor and can, therefore, promote photocatalytic processes at its interface.¹ TiO_2 absorbs in the ultraviolet spectrum, but can be photosensitized by the adsorption of chromophores that, when excited, inject electrons into the TiO_2 conduction band. These properties, in addition to its abundance, low cost, stability, and low toxicity, are the basis for its use in solar cells,² as a support for heterogeneous catalysts³ and photocatalysts,^{4,5} as a white pigment (where its photocatalytic activity leads to self-cleaning properties),⁶ and for disinfection,⁷ among other things.

To understand the photocatalytic activity of TiO_2 and the electronic processes occurring at the surface, one requires a good description of the electronic structure. The properties of TiO_2 surfaces have been the subject of a wide range of theoretical studies, which addressed the effect of introducing defects, usually oxygen vacancies, into the surface of TiO_2 ,^{8,9} the effect of cationic^{10,11} and anionic^{12,13} dopants on the electronic structure and associated properties; and the adsorption of molecules^{14,15} and metal atoms^{16,17} on the various surfaces of rutile and anatase forms of TiO_2 .¹⁸

In particular, many of the recent theoretical studies considered the adsorption of chromophores, molecules that absorb light in the visible range and readily inject electrons into the TiO_2 conduction band. These molecules can act as sensitizers so that light from the solar spectrum can promote electrons into the conduction band of TiO_2 .¹⁹ Many theoretical studies have focused on the adsorption of common anchoring groups (carboxylic acid,^{14,20–24} phosphonic acid,^{25,26} and hydroxyl

groups^{21,27–29}) of chromophores to TiO_2 surfaces. Carboxylic acid is one of the most common anchoring groups in chromophores, and several studies investigated the interaction of formic acid with the TiO_2 surfaces.^{14,20,22,23} Dissociative adsorption in the bridging bidentate configuration is the most favorable for formic acid on the rutile (110) surface,¹⁴ whereas both dissociatively and nondissociatively adsorbed structures are believed to be stable on anatase (101) surfaces.²⁰ A study of the adsorption of oxalate/oxalic acid, COOH_2 , onto rutile nanocrystals found various stable binding configurations, some of which are not available to the RCOOH chromophores.²⁴ There were very few studies concerned with the adsorption of larger carboxylic acid molecules, such as benzoic acid,²¹ which perhaps provide a better model of the chromophore–surface interaction. Therefore, one of the aims of this paper is to model the adsorption of benzoic acid on TiO_2 surfaces and to study its effect on the electronic structure of TiO_2 .

The majority of applications of TiO_2 involve the photoexcitation of an electron into the conduction band of TiO_2 . As a result, to correctly model the physics essential in these applications, it is important to model the band gap and any band-gap states correctly. A number of density functional theory (DFT) methods have been explored to study the electronic structure of TiO_2 and the effect of using different functionals on the resulting band gap. Hybrid functionals have been shown to provide a band gap closer to experiment and more accurately represent the localization of gap states created by oxygen vacancies.³⁰ The almost ubiquitous B3LYP functional³¹ has been found to give a good estimate of the band gap for TiO_2 ; the less commonly used PBE0 functional³² gives an excellent description of the structure, though it overestimates the band gap considerably.³³ Pure GGA functionals are also commonly employed in studies of TiO_2 and produce band structures that are in qualitative agreement with those obtained using hybrid functionals. However, the band gap is significantly underestimated,^{33–35} and the GGA methods tend to artificially delocalize

* To whom correspondence should be addressed. E-mail: N.Martsinovich@warwick.ac.uk

the electron density so that defect states are sometimes qualitatively incorrect (for example, the energies of gap states of an oxygen vacancy in TiO_2 are overestimated and are found in the conduction band).³⁰ Several attempts have been put forward to improve the band-gap description of TiO_2 , including the ad hoc methods of scissor operators^{28,36} and tuning the exact exchange.³⁴ The more rigorous DFT + U method, which uses an electron repulsion term, U , to correct for the tendency of pure DFT to delocalize the electron density, has the disadvantage that the transferability of the U parameters is undetermined,³⁵ and indeed, the optimal value of U in the simulation of TiO_2 varies between functionals and implementations.^{37–40}

It is customary for comparative studies of solid-state electronic structures to consider different density functionals without changing the other characteristics of the calculation (e.g., plane-wave or localized basis set, all-electron or pseudopotentials) because, in general, this allows the use of a single code to perform all the computations. However, different implementations of DFT have different characteristics in terms of convergence, computational stability of the results, and accuracy. In particular, the computation of two-dimensional surfaces using plane waves and pseudopotentials, which is becoming standard for highly accurate computations,^{41–44} requires much larger computational resources compared with the calculations using localized basis sets, particularly because the vacuum between layers is filled with basis functions that require the same computer time as the solid to model.

In this paper, we will, therefore, explore the effect of three different DFT implementations on the electronic structure of several TiO_2 surfaces, with and without molecular adsorbates, comparing computational cost and accuracy for different density functionals. The details of the implementations are given in section 2. As this paper deals with comparisons between these DFT implementations, throughout this work, the phrase “DFT method” means the complete choice of software, basis set, and pseudopotential. In section 3.1, we describe computations of 2D slabs of rutile exposing the (110) surface and anatase exposing the (101) surface. The surface energy, band gap, partial density of states, and relaxation computed using the three methods for slabs of various thicknesses are compared. In section 3.2, we then consider the adsorption of benzoic acid on rutile (110) and anatase (101) surfaces and, in particular, the effect of the adsorbate on the density of states of the rutile and anatase slabs. This paper concludes by reviewing the role of the electronic density of states in calculating the rates of electron-transfer processes.

2. Methods

2.1. DFT Techniques. We performed DFT calculations and compared the results given by three DFT methods based on different approaches: (i) all-electron calculations with localized Gaussian basis sets (using CRYSTAL06⁴⁵), (ii) pseudopotential calculations with localized basis sets (using SIESTA⁴⁶), and (iii) pseudopotential calculations with plane-wave basis sets (using PWSCF distributed within the Quantum ESPRESSO suite of codes^{47,44}). All of these calculations were done within the GGA approximation using the Perdew–Burke–Ernzerhof (PBE)⁴⁸ exchange-correlation functional; CRYSTAL06 bulk calculations were also done using several alternative functional, the localized density approximation (LDA) functional,⁴⁹ the Perdew–Wang (PW) GGA functional,⁵⁰ the PBE0³² hybrid functional, and the B3LYP hybrid functional.³¹ The B3LYP functional is not available in all software, and hybrid functionals generally are expensive when using plane-wave basis sets, but it has previ-

ously been shown to give a good description of the band gap of TiO_2 and is widely used for describing molecular systems.

CRYSTAL06 computations employed an explicit all-electron representation of the TiO_2 with a triple valence plus polarization Gaussian basis set first used in refs 51 and 52. The k -points sampled were chosen using a Monkhorst–Pack net using $4 \times 4 \times 4$ k -points for the bulk TiO_2 , $4 \times 4 \times 1$ k -points for clean slabs, and $2 \times 2 \times 1$ k -points for slabs with adsorbates. Default optimization criteria have been used for geometry optimization and electronic self-consistency (similarly in SIESTA and Quantum ESPRESSO calculations, below). To achieve convergence of the self-consistent field (SCF), a mixing weight of 0.05 and the Anderson mixing scheme^{53,54} were employed. To achieve convergence of the surface energy with slab depth, an extrafine integration scheme identical to that used in ref 55 was used. In calculations of adsorption using CRYSTAL and SIESTA, basis set superposition error (BSSE) was corrected using the counterpoise scheme.⁵⁶

SIESTA calculations used the PBE functional⁴⁸ and (for bulk TiO_2) the Wu and Cohen functional (WC)⁵⁷ (a modification of the PBE functional for improved description of solid state) and Troullier–Martins norm-conserving relativistic pseudopotentials provided on the SIESTA web page.⁵⁸ Specifically, we used the Ti and O pseudopotentials proposed in ref 59, where the semicore states (3s, 3p) for Ti are treated explicitly. A double- ζ -polarized (DZP) basis was used for all atoms, except for Ti semicore states, for which a minimal (single- ζ) basis was used. Convergence of the bulk rutile total energy and band gap was tested with respect to the k -point grid and to the mesh cutoff (energy cutoff for the real space grid used to represent the electron density), and the converged values were used in all SIESTA calculations: 150 Ry mesh cutoff and 10 Å k -point grid cutoff. This k -grid cutoff gives $4 \times 7 \times 1$ and $4 \times 6 \times 1$ k -grids for clean rutile and anatase slabs, respectively, and $4 \times 3 \times 1$ or $3 \times 3 \times 1$ k -grids for slabs with adsorbates. SIESTA SCF calculations used the Pulay mixing procedure with the mixing weight of 0.1 for bulk cells and small slabs. For large slabs (five or more layers) and slabs with adsorbates, the SCF procedure often diverged, and lower mixing weights (0.05 or 0.02) were needed. Also, the number of previous input and output density matrices used to create a new density matrix was increased from three to five to ensure convergence.

PWSCF calculations employed the GGA PBE functional⁴⁸ and ultrasoft pseudopotentials⁶⁰ provided on the Quantum ESPRESSO web page.⁴⁷ Semicore states were included in the Ti pseudopotential. Convergence of bulk rutile and anatase energies was tested with respect to the kinetic energy cutoff and the k -point grid, and the converged cutoff and k -point density were used in all following calculations. The kinetic energy cutoff for wave functions was 35 Ry and, for charge density, 280 Ry. The $4 \times 8 \times 2$ and $4 \times 4 \times 2$ k -point grids were used for clean rutile and anatase slabs, respectively, and a $2 \times 2 \times 1$ grid for slabs with adsorbates. We checked that increasing the k -grid for these slabs does not significantly affect molecular adsorption energies (≤ 0.1 eV difference) and band gaps (≤ 0.002 eV difference). PWSCF simulations converged using the Broyden mixing weight of 0.25, even for large slabs.

2.2. Systems. Bulk rutile and anatase, the most stable TiO_2 polymorphs, were modeled using conventional unit cells: 6 atoms for rutile and 12 atoms (two primitive cells) for anatase. Bulk lattice parameters were relaxed using lattice optimization procedures provided in the DFT codes; the positions of atoms

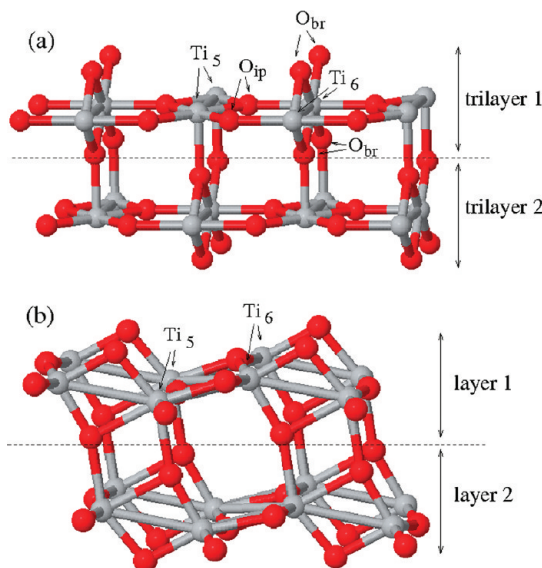


Figure 1. (a) A two-layer rutile and (b) a two-layer anatase slab (both are unoptimized 2×2 cells). In-plane and bridging O atoms (O_{ip} , O_{br}) are highlighted in the rutile slab and 5- and 6-coordinated Ti atoms (Ti_5 , Ti_6) in both slabs.

in the unit cells were relaxed simultaneously with the lattice parameter optimization.

Rutile (110) and anatase (101) slabs were constructed from six-atom primitive (TiO_2)₂ unit cells. Thus, we define a rutile (110) layer as a trilayer consisting of two in-plane Ti, two in-plane O atoms, and two bridging O atoms above and below the central Ti–O layer. Similarly, an anatase (101) layer contains two Ti and four O atoms in its primitive unit cell; all of these atoms have different z coordinates (Figure 1). We considered both free (unconstrained) slabs and slabs with a fixed bottom layer. For the SIESTA and Quantum ESPRESSO computations, the slabs were separated by 10 Å of vacuum.

We used two approaches to model molecular adsorption on surfaces: (i) constrained slabs with the adsorbate placed at one side of the slab, and one or several bottom layers fixed, as used in the majority of simulations of surfaces, including TiO₂ (e.g., ref 20), and (ii) free slabs (no constrained atoms) with adsorbates placed symmetrically on the top and bottom surfaces of the slab, used in studies of molecular adsorption on rutile (e.g., ref 14). It has been reported that, thanks to the symmetry of the system, the latter systems converge more quickly than the former, despite the larger number of atoms in the free-slab systems. The latter approach also avoids fixing bottom layers of the slab, which affects the electronic structure of the slabs.

Two adsorption geometries were considered for benzoic acid on anatase (101): dissociative adsorption in the bridging bidentate geometry and nondissociative molecular adsorption. Only dissociative adsorption of the molecule was considered on the rutile (110) surface. Two- to four-layer anatase and two- to five-layer rutile slabs were used, either free or with a fixed bottom layer. The surfaces were modeled by periodic (1×3) surface unit cells. We verified that this cell size provided sufficient separation between molecules in neighboring cells and there was no or minimal interaction between the molecules. The interaction energy between isolated benzoic acid molecules at this separation is negligible (≤ 0.05 eV). The periodic cells and intermolecular distances are shown schematically in Figure 2. The periodic arrangement of the cells was varied (see Figure 2); this was found to have little effect on binding energies (within 0.1 eV) and on the electronic structure.

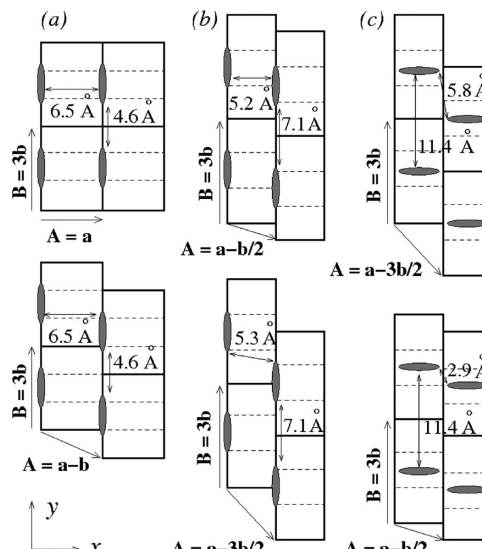


Figure 2. Schematic showing top views of (a) rutile and (b, c) anatase cells used in the calculations of (a, b) dissociated and (c) undissociated benzoic acid adsorption, and periodic arrangements of the cells used in our calculations. Rectangles (thick solid lines) show the (1×3) cells; thin dashed lines show primitive (1×1) surface cells within these (1×3) cells. Shaded ovals show the positions of benzoic acid molecules. Intermolecular distances are shown. There is one molecule per (1×3) cell. Lattice vectors \mathbf{A} and \mathbf{B} of the (1×3) cells are indicated and expressed via the lattice vectors \mathbf{a} and \mathbf{b} of the primitive (1×1) cells ($\mathbf{a} = 6.56$ Å, $\mathbf{b} = 2.98$ Å for rutile (110) cells; $\mathbf{a} = 5.19$ Å, $\mathbf{b} = 3.82$ Å for anatase (101) cells). The top left arrangement of cells is rectangular; the rest of the cell arrangements are oblique. The cells shown in the upper row were used in most of the calculations; the cells in the lower row were used to test convergence with respect to intermolecular distances.

3. Results

3.1. Rutile (110) and Anatase (101) Surface Computations. For consistency, the bulk structure used to generate the initial geometry of the various slabs considered here needs to be optimized with the same method and parameters, and therefore, the optimization of bulk TiO₂ (rutile and anatase) constitutes a required preliminary work. Bulk TiO₂ has been studied many times with a variety of methods,^{61–63,34,33} and our bulk optimized structure and band gaps match those reported in the literature with analogous methods. For completeness, and to allow easier comparison with the slab results, we report the results of the bulk calculations in Table 1. As already noted in the literature, although the predicted geometry is generally good, the band gap is significantly underestimated by the LDA and GGA approximations and somewhat overestimated by hybrid functionals (PBE0 and B3LYP).

The TiO₂ slabs were generated from the optimized bulk geometry exposing the most thermodynamically stable surface: (110) in the case of rutile and (101) in the case of anatase, and the atom coordinates were fully optimized. We consider the variation of the band gap, geometric relaxation, and surface energy with both the depth of the slab (varied between 2 and 10 layers) and the DFT method employed using the PBE functional with each method. A comparison is also made between the PBE functional and the B3LYP functional using CRYSTAL06.

3.1.1. Electronic Structure. The variation of the band gap of the rutile (110) and anatase (101) slabs with the number of layers for the three DFT methods used is presented in Figure 3. As has been observed previously,⁶⁶ the band gap for the rutile (110) slabs oscillates around the bulk value.

TABLE 1: Geometric Parameters for Rutile and Anatase Computed Using a Variety of DFT Methods Compared with Experiment^{64,65} and Hartree–Fock Computations

functional	rutile				anatase			
	<i>a</i> /Å	<i>c</i> /Å	<i>u</i>	band gap/eV	<i>a</i> /Å	<i>c</i> /Å	<i>u</i>	band gap/eV
CRYSTAL06								
LDA	4.556	2.936	0.304	1.82	3.755	9.473	0.2081	2.31
PBE	4.644	2.982	0.305	1.87	3.806	9.742	0.2060	2.39
PW	4.637	2.979	0.305	1.88	3.802	9.723	0.2060	2.40
PBE0	4.585	2.963	0.305	4.10	3.773	9.623	0.2058	4.58
B3LYP	4.628	2.982	0.306	3.58	3.794	9.754	0.2049	3.98
Hartree–Fock	4.567	2.992	0.306	12.21	3.780	9.656	0.2044	12.79
SIESTA								
PBE	4.637	2.998	0.305	1.72	3.800	9.773	0.206	2.29
WC	4.595	2.957	0.304	1.72	3.794	9.469	0.209	2.24
Quantum ESPRESSO								
PBE	4.618	2.949	0.306	1.86	3.791	9.653	0.207	2.12
experiment	4.593	2.958	0.305	3.03	3.789	9.522	0.208	3.3

Slabs with an odd number of layers have a band gap smaller than the bulk value, whereas slabs with an even number of layers have a band gap larger than the bulk value. Both odd- and even-thickness slabs appear to converge on the bulk band gap for all DFT methods and both DFT functionals considered (≈ 1.85 eV for PBE, ≈ 3.7 eV for B3LYP). The agreement between the three DFT methods using the PBE functional for the rutile (110) slabs is very good; the maximum discrepancy between the methods is 0.12 eV for the seven-layer slab.

The oscillations in the electronic and structural properties of rutile (110) slabs are well-known^{67,66} and have been attributed to the change in hybridization of the O 2p and Ti 3d states: in even-layered slabs, the O–Ti hybridization causes the formation of tightly bound TiO_2 bilayers, whereas in odd-layered slabs, which have a symmetry plane in the middle, the O(2p)–Ti(3d) hybrid orbitals extend across the entire slab.⁶⁶ These oscillations are an intrinsic property of rutile (110) surfaces and do not occur in other rutile or anatase surfaces.

Unlike the rutile (110) slabs, the anatase (101) band gap converges monotonically on the bulk value. The difference of ≈ 0.2 eV between the CRYSTAL06 computations and the other two codes is consistent for all slab thicknesses and may be attributed to the use of pseudopotential cores in the CRYSTAL06 computation. There are no surface states created by the rutile (110) or anatase (101) surfaces.

To compare the electronic structure of the various slabs computed using CRYSTAL06 with the B3LYP and PBE functionals, the proportion of the density of states (DOS) on the atoms of each layer is compared in Figure 4 for rutile

(110) slabs. Aside from the shift in energy of the conduction band edge, the distribution of states in the valence and conduction bands for each slab thickness is similar for both functionals. Near the conduction band edge, the majority of states has the largest amplitude on the subsurface layer of the slab, and on the third subsurface layer in thicker slabs. Thus, for the three- and seven-layer slabs, the conduction band edge is dominated by their central layer.

A similar plot displaying the proportion of the density of states localized on each layer of the anatase (101) slabs is shown in Figure 5. Compared with the rutile (110) slabs, the states in the conduction and valence bands are distributed more evenly between the layers. Like the rutile (110) slabs, the conduction band edge has fewer states on the surface atoms than those beneath the surface.

3.1.2. Surface Energies and Slab Geometries. The surface energies for these slabs are shown in Figure 6. The oscillations between odd and even are apparent in the surface energies of the rutile (110) slabs. The energy appears to converge on ≈ 0.53 J m⁻² for both methods employing localized basis functions and ≈ 0.35 J m⁻² for the plane-wave computations using Quantum ESPRESSO. The choice of pure or hybrid functional using CRYSTAL06 has little effect on the surface energy. The surface energies of the anatase (101) slabs converge monotonically; similar to the case of the anatase slabs' band gap, there is no distinction between odd- and even-thickness slabs. As in the case of the rutile (110) slabs, the surface energy computed using Quantum ESPRESSO (0.44 J m⁻²) is smaller than that computed using the two localized basis sets methods by ≈ 0.2 J m⁻².

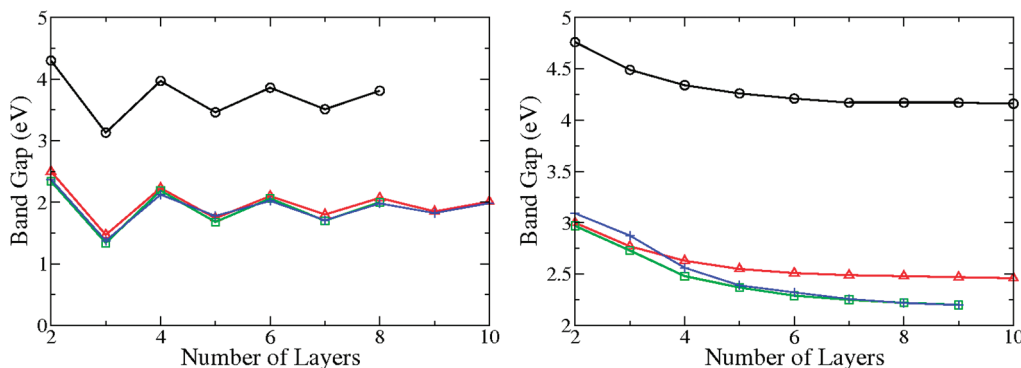


Figure 3. Band gap computed for (left) rutile (110) and (right) anatase (101) slabs using CRYSTAL06 with PBE (triangles) and B3LYP (circles), SIESTA (squares), and Quantum ESPRESSO (plus).

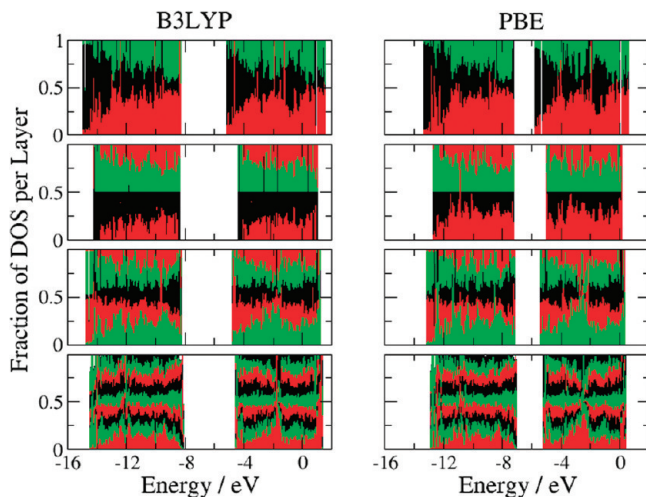


Figure 4. Relative density of states for atoms by layer for (from top to bottom) three-, four-, five-, and nine-layer rutile (110) slabs computed using CRYSTAL06 with B3LYP (left) and PBE (right). Each color represents a layer arranged in order of their z coordinate; the width of a particular section is the fraction of the DOS that layer contributes.

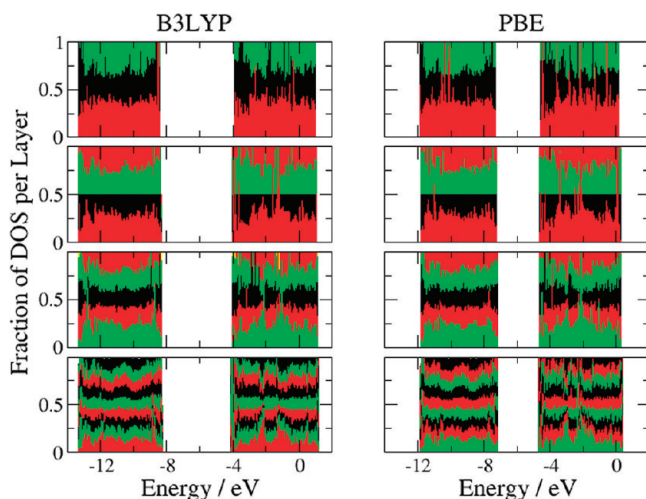


Figure 5. Relative density of states for atoms by layer for three-, four-, five-, and nine-layer anatase (101) slabs computed using CRYSTAL06 with B3LYP (left) and PBE (right). Represented as in Figure 4.

There is no agreement in the literature on the values of the TiO₂ surface energies. The studies using localized atomic orbitals report values in the range of 0.42–0.68 eV for rutile (110),^{66,55} in agreement with our values. It has also been noted that the calculated values of surface energies strongly depend

on the computational method used (density functional, value of U in DFT + U calculations).^{40,55} The low values obtained in our plane-wave calculations are consistent with earlier studies of rutile (110)⁶⁸ and anatase (101),^{62,69} which also used plane waves together with ultrasoft pseudopotentials, with either the same code (in ref 62) or a different code (in refs 68 and 69). For comparison, plane-wave calculations with the projector augmented wave approach (PAW) gave a rutile surface energy of 0.58 J m⁻².⁴⁰ Thus, the low values of the Quantum ESPRESSO surface energies may be attributed to ultrasoft pseudopotentials.

The geometry of the rutile (110) slab relaxes noticeably from the bulk positions: the under-coordinated Ti atom sinks below the surface plane; the surface in-plane O atoms and 6-coordinated Ti move above the plane, in the opposite direction. Using B3LYP with CRYSTAL06, in the 10-layer slab, the under-coordinated Ti atom moves by -0.075 \AA and the O atoms move by 0.142 \AA . The O–Ti–O angles that are 90° in the bulk are 100.3° in the final geometry. The 6-coordinated Ti atom on the surface of the three-layer slab relaxes outward by 0.16 \AA . The surface relaxation is very similar in all slabs: the O–Ti–O angle in the three-layer slab is 99.1° , and the movement of the under-coordinated Ti atom is -0.06 \AA . The relaxation, especially of Ti atoms, is significant in all layers, up to deep subsurface layers. The relaxation of the geometry is qualitatively similar using all three codes; the choice of functional also appears unimportant in this case.

As discussed in the literature,^{70,66,55} the energy difference between the odd- and even-layered slabs is related to their relaxation and to the presence of the middle layer: in the case of the odd-layered slab, there is a plane of symmetry at the center of the cell, and the middle layer retains a geometry almost identical to that of the bulk, whereas in the even slabs, there is only a point of rotational symmetry at the center of the cell, and the absence of a middle layer ensures a greater flexibility of the slabs.

The optimized geometry of the anatase (101) slabs, when compared with the bulk geometry, shows significant displacement in the surface layer and the first subsurface layer; afterward, the maximum displacement from the bulk geometry is less than 0.07 \AA . The relaxation of atoms for the surface layers is captured well already in the three- and four-layer slabs. The difference in geometry computed using the PBE and B3LYP functionals is negligible.

3.1.3. Convergence of Slabs on “Surface-Like” Behavior. When TiO₂ is studied as an electron acceptor, it is important to establish how deep the slab needs to be in order to

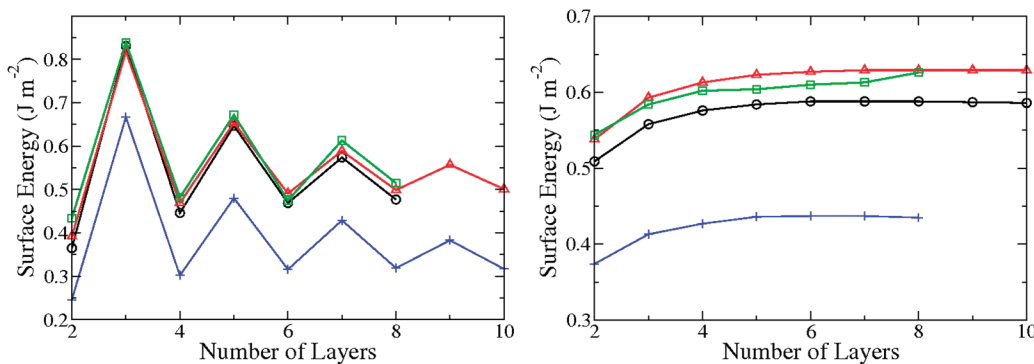


Figure 6. Surface energy computed for (left) rutile (110) and (right) anatase (101) slabs using CRYSTAL06 with PBE (triangles), SIESTA (squares), and Quantum ESPRESSO (plus).

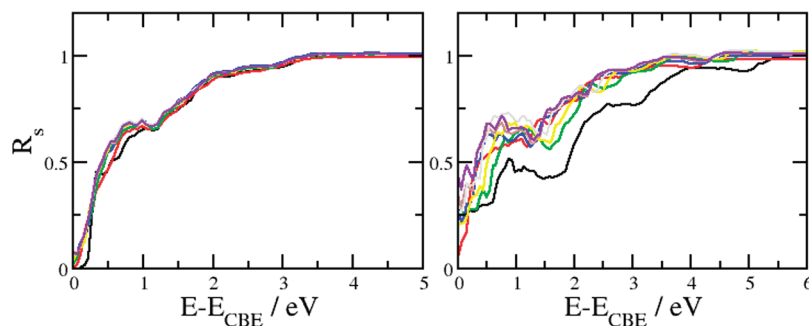


Figure 7. $R_s(E)$ against E for slabs computed using the B3LYP functional with CRYSTAL06 for anatase (101) (left) and rutile (110) (right) for slabs 3 (black), 4 (red), 5 (green), 6 (blue), 7 (yellow), 8 (brown), 9 (gray), and 10 (violet) layers thick.

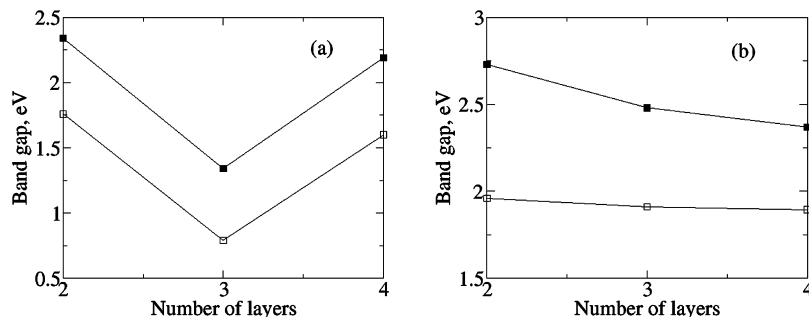


Figure 8. Band gap for (a) rutile (110) and (b) anatase (101) (computed with PBE). Filled symbols correspond to free slabs and empty symbols to constrained slabs.

represent accurately the conduction band local density of states of a true surface. We, therefore, compare the ratio of states per atom on the surface atoms and on other atoms in the slab. $R_s(E)$ is defined as

$$R_s(E) = \frac{\left\langle \int_{E_{CBE}}^E dE' \rho_i(E') \right\rangle_s}{\left\langle \int_{E_{CBE}}^E dE' \rho_i(E') \right\rangle_o} \quad (1)$$

wherein s and o represent surface Ti atoms and other Ti atoms in the cell, $\rho_i(E)$ is the partial density of states on atom i at energy E , E_{CBE} is the energy of the conduction band edge, and $\langle \rangle_s$ and $\langle \rangle_o$ denote the mean values over all surface Ti atoms and all other Ti atoms. $R_s(E) = 1$ means that the contribution of the surface layer atoms to the total DOS in the conduction band is equal to the (averaged) contribution of each of the subsurface layers. When $R_s(E) < 1$, the contribution of the surface layers to the total DOS (from the bottom of the conduction band to the energy E) is smaller than that of the bulk layers.

$R_s(E)$ against energy is plotted in Figure 7 using the CRYSTAL06 B3LYP computations of the rutile (110) and anatase (101) slabs. The figure shows that the conduction band edge states are localized away from the surface (as shown by the low values of R_s near $E = E_{CBE}$). The contribution of the surface states to the conduction band edge does not become as significant as the middle layers' until ≈ 4 eV above the band edge for anatase and ≈ 5 eV for rutile (close to the top of the conduction band). However, given the similarity of the curves for slabs of different thickness, it can be seen that even the three-layer anatase slab gives an appropriate model of the surface. For rutile surfaces, the convergence is less rapid and further complicated by the odd–even effects mentioned previously. The

rutile slabs with five or more layers appear very similar in terms of the $R_s(E)$ across this energy range.

The PBE results are almost identical to the B3LYP results shown in Figure 7. This, together with the similarity in the contributions to DOS shown in Figures 4 and 5, proves that, although the band gap is underestimated by GGA, the states in the conduction band of TiO_2 slabs are described by GGA correctly (or at least in a very similar way to the more accurate hybrid functional description).

3.1.4. Electronic Structure of Constrained Slabs. Calculations of adsorption on surfaces commonly use constrained slabs, where atoms in one or more bottom layers of the slab are not allowed to move. We investigated the effect of constrained layers on the band gap and density of states of the TiO_2 slabs. Both in rutile (110) and in anatase (101) slabs, the band gap is reduced by 0.4–0.8 eV in constrained slabs; see Figure 8. In the case of anatase slabs, convergence with the number of layers is much faster than for free slabs. In the rutile slabs, odd–even oscillations are still evident, like in the free slabs.

The analysis of the partial density of states of free and constrained slabs (shown in Figure 9) shows the origin of this change in the band gap: the states on fixed O atoms (and, to a smaller extent, fixed Ti atoms) are found at higher energies than those of unconstrained O atoms and now form the top of the valence band (clearly seen as a shoulder at the top of the valence band of the rutile slab in Figure 9). Thus, the valence band maximum is shifted upward. The states on fixed 5-coordinated Ti atoms also dominate the bottom of the conduction band in anatase slabs and may shift the conduction band minimum slightly downward.

Thus, the valence band maximum (VBM) shift in constrained slabs is due to the fixed bottom layers and should not affect adsorption and electron transfer into the top layers. However, it is important to keep in mind the origin of these changes in the band gap when comparing the electronic structure of

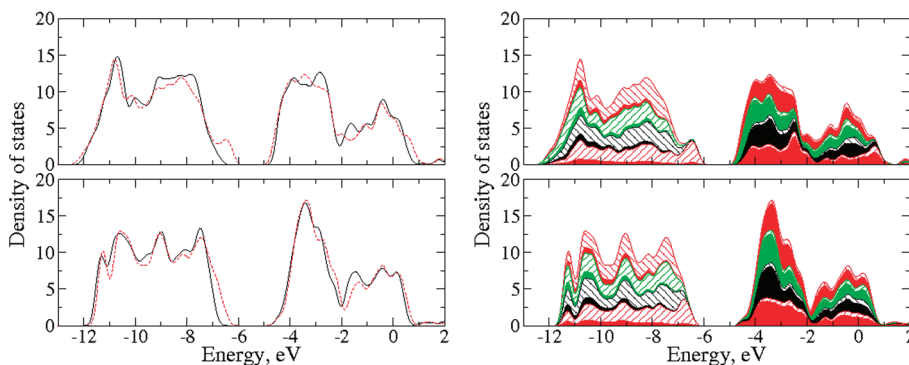


Figure 9. Left panel: total density of states for four-layer rutile (110) (top image) and four-layer anatase (101) slabs (bottom image). Solid lines, free slabs; dashed lines, constrained slabs. Right panel: contributions of partial densities of states for Ti and O atoms layer by layer to total DOS for the constrained four-layer rutile (110) (top image) and anatase (101) (bottom image) slabs. Shaded areas represent Ti atoms' contributions, and hatched areas are O atoms' contributions. All computed using SIESTA.

TABLE 2: CPU Time for Geometry Optimizations of Bulk Anatase, a Four-Layer (101) Slab and an Eight-Layer (101) Slab using CRYSTAL06, with PBE and B3LYP, Quantum ESPRESSO, and SIESTA^a

method	bulk/s	four-layer slab/s	eight-layer slab/s
CRYSTAL06			
PBE	943 (8)	27 949 (17)	57 668 (17)
B3LYP	6 163 (7)	171 201 (19)	370 848 (20)
SIESTA			
PBE	1 001 (5)	14 154 (42)	95 352 (69)
Quantum ESPRESSO			
PBE	564 (37)	128 580 (38)	673 080 (30)

^a The number of geometry optimization steps in each calculation is given in parentheses.

constrained slab–adsorbate systems (e.g., discussed later in the paper) with bulk rutile or anatase.

3.1.5. Relative Computational Cost. When comparing the results obtained by different software, it may be interesting to compare also the relative computational cost of the corresponding calculations. It is important to stress that it is not easy to rank the codes on the basis of their efficiency. The total optimization time reflects both the efficiency of the minimum energy search and the efficiency of the electronic structure calculation (different for the three codes). Moreover, some codes, such as CRYSTAL06, albeit not the fastest in serial calculations, provide a massively parallel version, whereas another rapid code, SIESTA, has a parallel version with poorer scaling properties. However, as a term of reference, it is useful to indicate the computer time and the number of iterations required to optimize two representative systems (a four-layer slab and an eight-layer slab). Table 2 reports the CPU time for optimization of the bulk anatase from the X-ray structure⁶⁴ and for the optimization of the four-layer and eight-layer anatase slabs from the bulk geometry, together with the number of geometry optimization steps for each of the calculations. The computations were run on a single processor on Intel(R) Xeon(R) 2.66 GHz machines with 16 GB RAM.

It is clear from Table 2 that the more accurate band gap computed using the hybrid B3LYP functional comes at a high computational cost. Computations using this functional take about 6 times as long as the equivalent computations using the pure GGA functional. It is also apparent that the CRYSTAL06 computations, despite treating all electrons explicitly, are fastest, although closely competing with SIESTA in computation times. Given that no significant differences between the DOS computed using the various methods were found, we can confidently use

the least computationally expensive and most stable combination of software and methodology to model the TiO₂ surfaces.

3.2. Adsorption of Benzoic Acid on the TiO₂ Surfaces.

Benzoic acid is a common anchoring group in chromophores used in dye-sensitized solar cells (DSSCs). To investigate its effect on the density of states of TiO₂ slabs, we model adsorption of benzoic acid on rutile (110) and anatase (101) surfaces using localized basis set (SIESTA) and plane-wave (Quantum ESPRESSO) PBE calculation. For thin slabs (two and three layers), we also perform calculations using the B3LYP hybrid functional (CRYSTAL), to evaluate the effect of the functional on the electronic structure. We consider benzoic acid dissociatively adsorbed in the bridging bidentate geometry on the rutile (110) surface and both dissociative and nondissociative adsorption of benzoic acid on anatase (101) surfaces—the most stable adsorption configurations on these surfaces.^{14,20}

3.2.1. Adsorption Geometries and Energies. Dissociated Benzoic Acid on Rutile. The benzoate anion adsorbs on the rutile (110) surface in an upright geometry (perpendicular to the surface), as shown in Figure 10a. The details of the final structures obtained using all three DFT methods are very similar. The Ti–O bond lengths between the carboxylate oxygens and the surface titanium atoms are 2.03–2.10 Å, slightly longer than Ti–O distances in the bulk rutile (1.95–2.00 Å) and Ti–O distances involving 5-coordinated Ti atoms of the bare surface (these range between 1.78 and 1.97 Å), but close to Ti–O distances between 6-coordinated surface Ti atoms and in-plane oxygens or below-the-plane bridging oxygens.

Adsorption of benzoic acid causes considerable displacements of slab atoms. In particular, 5-coordinated Ti atoms, which are sunken slightly below the surface level in the bare rutile (110) slabs, rise by 0.13–0.22 Å as a result of bonding to O atoms of the benzoate ion (a smaller displacement in the even-layered slab and larger displacements in odd-layered slabs) and adopt positions close to the ideal bulk termination of the surface. Subsurface Ti and O atoms also move from their slab positions by up to 0.16 Å, mainly up or down along the vertical direction.

Adsorption energies (Figure 11) show odd–even oscillations depending on the number of layers in the slab: they vary between –0.7 and –2.0 eV per molecule (larger absolute values for odd-layered slabs, smaller values for even-layered slabs) and follow a similar trend in both constrained and free slabs. Adsorption energies predicted by plane-wave PBE calculations agree very well (within 0.05 eV) with the B3LYP results (obtained for two- and three-layer slabs) and are up to 0.2 eV larger than the values found using SIESTA. The periodic arrangement of the cells (see Figure 2) was found to have little effect on adsorption energies

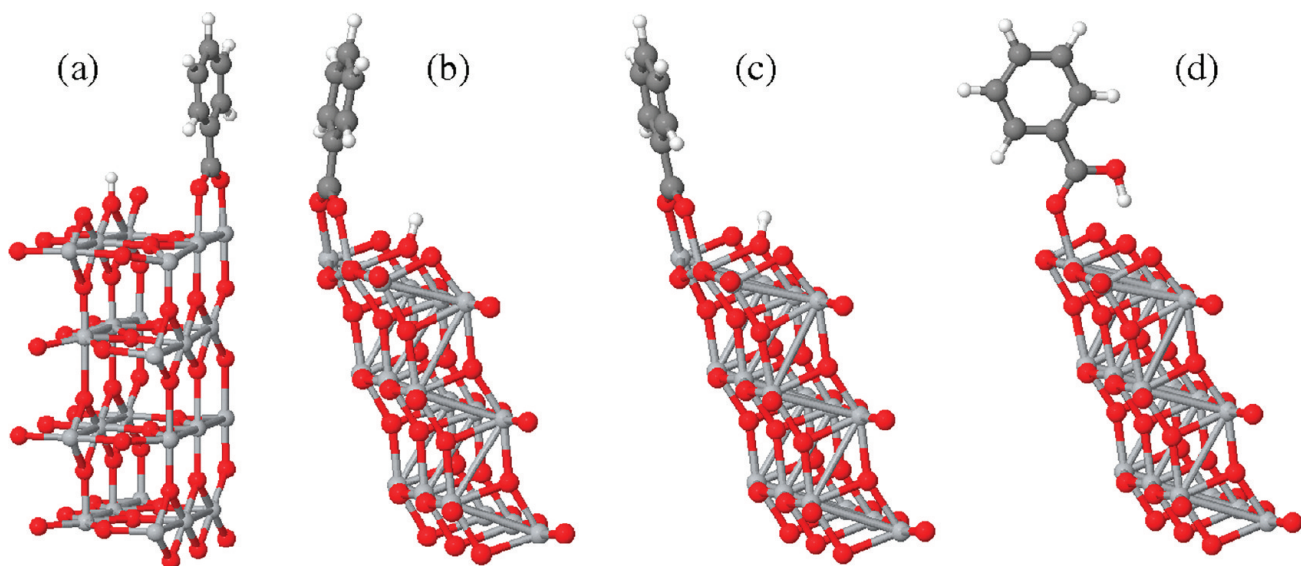


Figure 10. Adsorption geometries: (a) dissociated benzoic acid on rutile; (b, c) dissociated benzoic acid on anatase, geometries A and B; and (d) nondissociated benzoic acid on anatase.

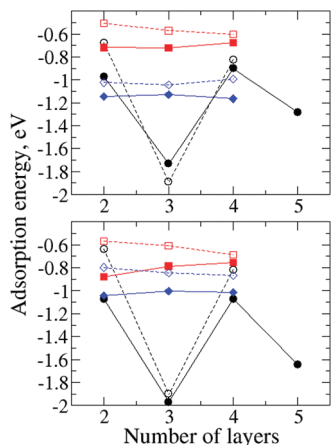


Figure 11. Adsorption energies of benzoic acid on rutile and anatase surfaces. Top panel: SIESTA results. Bottom panel: Quantum ESPRESSO results. Black circles, dissociated benzoic acid on rutile (110); red squares, dissociated benzoic acid on anatase (101); blue diamonds, nondissociated benzoic acid on anatase (101); full lines with filled symbols, adsorbate on constrained slabs; dashed lines with empty symbols, adsorbate on free slabs. The figure shows oscillations in adsorption energies of benzoic acid on rutile (110) and nearly constant adsorption energies on anatase (101).

(within 0.1 eV) for rutile and anatase. Convergence of adsorption energies is very slow and is not reached in slabs of this size. From the data in Figure 11, we expect converged adsorption energies to be between -1.0 and -1.4 eV. For comparison, an earlier study,¹⁴ which used five- or six-layer slabs, found the value of the adsorption energy of formic acid on rutile to be -190 kJ mol⁻¹ (-2.0 eV),¹⁴ close to our larger adsorption energies.

Dissociated Benzoic Acid on Anatase. The benzoate anion adsorbs on the anatase (101) surface in a tilted geometry. Two stable geometries with different tilt angles were found; both are shown in Figure 10b,c. In structure A, the Ti–O bonds form a $61\text{--}62^\circ$ angle with the $z = 0$ plane, while the molecule itself forms a $97\text{--}98^\circ$ angle with this plane (the molecule pivots around its O atoms). In structure B, there is no such change in angle: the molecule forms a 76° angle with the $z = 0$ plane. The distances between the carboxylate oxygens and the surface

titanium atoms are $2.11\text{--}2.15$ Å in both structures, longer than Ti–O distances in the bulk anatase ($1.95\text{--}2.0$ Å) and the anatase (101) surface and slightly longer than the same distances for the benzoate adsorbed on rutile, due to the longer Ti–Ti distance in the anatase surface than in the rutile surface.

Adsorption of the benzoate ion also causes displacements of the surface and subsurface atoms. In particular, surface Ti atoms bonded to the ion move upward by $0.13\text{--}0.17$ Å (by a smaller amount in the thinner slab), and the surface O atom that bridges these Ti atoms flips and moves down by $0.49\text{--}0.53$ Å; subsurface Ti and O atoms also move by smaller amounts (up to 0.15 Å).

Adsorption energies are almost independent of the number of layers in the anatase slabs; they are slightly smaller for free slabs (-0.7 to -0.5 eV) than for constrained slabs (-0.9 to -0.6 eV); the latter values agree well those reported earlier in a study of formic acid on a two-layer anatase slab.²⁰ Again, the agreement between PBE and B3LYP binding energies is very good (up to 0.1 eV difference between B3LYP CRYSTAL and Quantum ESPRESSO results). Structure B is marginally more stable than structure A (by up to 0.1 eV). These energies show that dissociated benzoic acid is less strongly adsorbed on anatase (101) than on rutile (110).

Nondissociated Benzoic Acid on Anatase. Nondissociated benzoic acid adsorbs on anatase in an upright geometry, forming one Ti–O covalent bond and an additional O···H hydrogen bond. Only PBE calculations were done for this system: SIESTA calculations predict slightly shorter bond lengths (2.09–2.13 Å for Ti–O and 1.28–1.32 Å for O···H) than Quantum ESPRESSO (2.16–2.21 and 1.44–1.47 Å, respectively).

Consequently, SIESTA predicts slightly stronger binding than Quantum ESPRESSO (see Figure 11), but the difference in adsorption energies is no more than 0.2 eV, within the accuracy of DFT. Adsorption energies are -1.0 to -0.8 eV (free slabs) or -1.1 to -1.0 eV (constrained slabs). These energies show that benzoic acid adsorbs on anatase more strongly in the nondissociated form than in the dissociated form, in agreement with the earlier study of adsorption of formic acid.²⁰

Similar to the dissociated benzoic acid on anatase, adsorption energies are almost independent of the number of layers in the slabs. This suggests that even slabs as small as two layers (e.g., used in ref 20) can give a reasonable description of adsorption

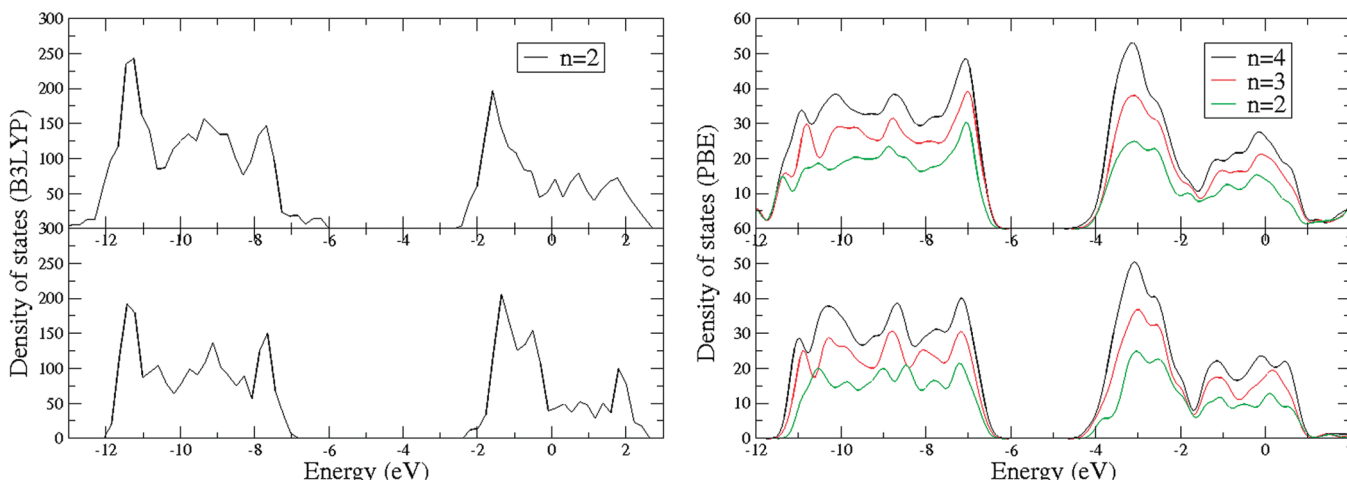


Figure 12. Left panel: density of states of a fully relaxed two-layer anatase slab (top) with and (bottom) without adsorbed dissociated benzoic acid, calculated using B3LYP. The adsorbate state appears above the valence band edge. Right panel: density of states of fully relaxed two-, three-, and four-layer anatase (101) slabs (top) with and (bottom) without adsorbed dissociated benzoic acid, calculated using PBE (SIESTA). The density of states for slabs with nondissociatively adsorbed benzoic acid (not shown) is almost identical to the results for the dissociatively adsorbed molecule shown here. The graphs are aligned at the positions of O 2s core levels.

of benzoic acid and similar molecules on anatase (101). This is very different from adsorption on rutile, where there is little evidence of convergence of adsorption energies with the number of layers. This makes it difficult, at least on the grounds of adsorption energies, to choose a small slab that is representative of the true rutile (110) surface.

3.2.2. Electronic Structure of Anatase (101) and Rutile (110) with Adsorbates. We compared band gaps and densities of states (DOS) for rutile and anatase slabs with adsorbed benzoic acid, to find out how adsorption affects the electronic structure of the TiO_2 slabs.

Anatase Slabs with Adsorbate. First, we compared the band gaps of anatase slabs with and without adsorbate, to get a picture of the effect of adsorption on the electronic structure of the slabs. Using PBE, the values of band gaps of the slabs with both dissociatively and nondissociatively adsorbed benzoic acid are very similar to those of the bare slabs shown earlier in Figure 8 and follow the same trend with respect to the number of layers, when both free and constrained slabs are used. The band gaps are reduced by 0.1–0.2 eV upon adsorption, in both plane-wave and localized basis set calculations. This suggests little effect of adsorbate on the electronic structure of anatase slabs. There are no energy levels in the gap due to benzoic acid; the highest occupied molecular orbital (HOMO) of benzoic acid is slightly below the valence band edge, and its lowest unoccupied molecular orbital (LUMO) is ~0.5 eV above the conduction band edge.

There is no change in the anatase band gap in B3LYP calculations of constrained slabs, but the situation is different for the free slab: states localized on the benzoic acid molecules appear ~0.8 eV above the conduction band edge (see Figure 12).

Analysis of the partial DOS of free and constrained slabs shows that the benzoic acid HOMO appears above the states of free TiO_2 oxygen atoms, but below fixed oxygen atoms' states in constrained slabs, and is thus obscured by the fixed atoms' states. This shows that, without the analysis of partial DOS, calculations using constrained slabs can give misleading results on the electronic structure of anatase—adsorbate systems. Similarly, PBE calculations underestimate the position of the benzoic acid HOMO and place it in the valence band.

We note that an earlier study of benzoic acid on anatase²¹ found no adsorbate-related levels in the gap. However, that study

used unrelaxed TiO_2 clusters, and benzoic acid levels were likely obscured by the fixed surface atoms' states.

Apart from the appearance of the gap state, the DOS for slabs with adsorbate are very similar to those of bare slabs, as shown in Figure 12. There are only small changes due to the presence of the adsorbate. States on Ti atoms bonded to the molecule shift closer to the conduction band minimum (CBM) than the equivalent undercoordinated surface Ti atoms not bonded to the adsorbate; similarly, states on O atoms close to the binding site are slightly closer to the VBM. States on carboxylate oxygens of benzoic acid or a benzoate anion also appear close to the VBM, in both the PBE and the B3LYP calculations. As a result, the band gap is slightly reduced. We note that the composition of the conduction band is very similar in the PBE and B3LYP calculations.

The DOS of slabs with different thicknesses (two, three, and four layers) are qualitatively very similar to each other (see the right panel in Figure 12), suggesting that slabs as small as two layers thick can be used to model adsorption of benzoic acid and similar molecules on the anatase (101) surface.

Rutile Slabs with Adsorbate. Adsorption of benzoic acid on rutile (110) has a dramatic effect on the band gap of rutile slabs: although odd–even oscillations are still present, the amplitude of these oscillations is much smaller than in bare slabs (Figure 13). Specifically, the band gaps of even-layered slabs are similar both with and without the adsorbate, whereas the band gaps of odd-layered slabs are increased by 0.5–0.7 eV. This change in the band gap is due to a shift in the position of the CBM of odd-layered slabs. As Figure 13 shows, the plane-wave and the localized basis set PBE calculations give very similar values of band gaps for rutile with adsorbed benzoic acid. The same effect is observed also in B3LYP calculations (although the actual values of band gaps are larger).

Analysis of PDOS of the three-layer slab (Figure 14) shows that the energies of states on subsurface Ti atoms, which form the CBM in odd-layered bare slabs (seen as a small peak near the CBM in the free slab and as a shoulder peak in the constrained slab), are raised when the adsorbate is present. Thus, adsorption of benzoic acid disrupts the O–Ti hybridization in the slab because of the strong relaxation of the middle layer due to the interaction with the adsorbate (or with the two adsorbates in the case of the symmetric slab). The shift in the subsurface atoms' states is very pronounced in three-layer slabs

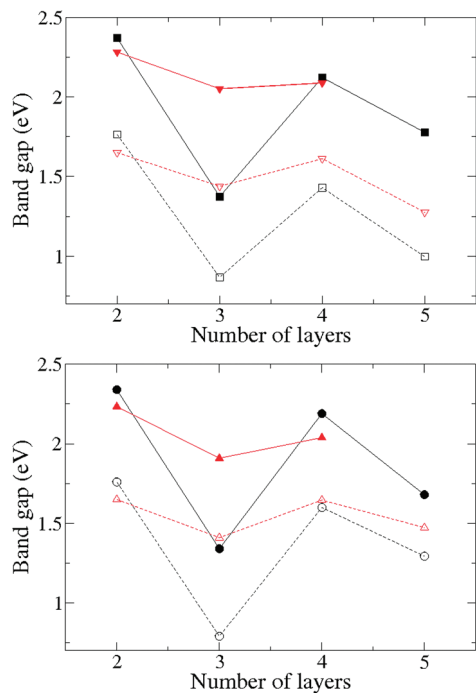


Figure 13. Band gaps of rutile slabs with and without adsorbed benzoic acid calculated using SIESTA (top panel) and Quantum ESPRESSO (bottom panel). Solid lines with filled symbols, free slabs; dashed lines with empty symbols, constrained slabs; squares or circles, bare slabs; triangles, slabs with dissociatively adsorbed benzoic acid.

but appears also in five-layer slabs, although significantly weakened thanks to the presence of the bulklike middle (subsubsurface) layer. By comparison, the small changes in the DOS of the even-layered slabs show that the TiO_2 bilayer formation described in ref 66 is not disrupted. These small changes correlate with smaller relaxations of Ti and O atoms in even-layered slabs upon adsorption, as mentioned in section 3.2.1.

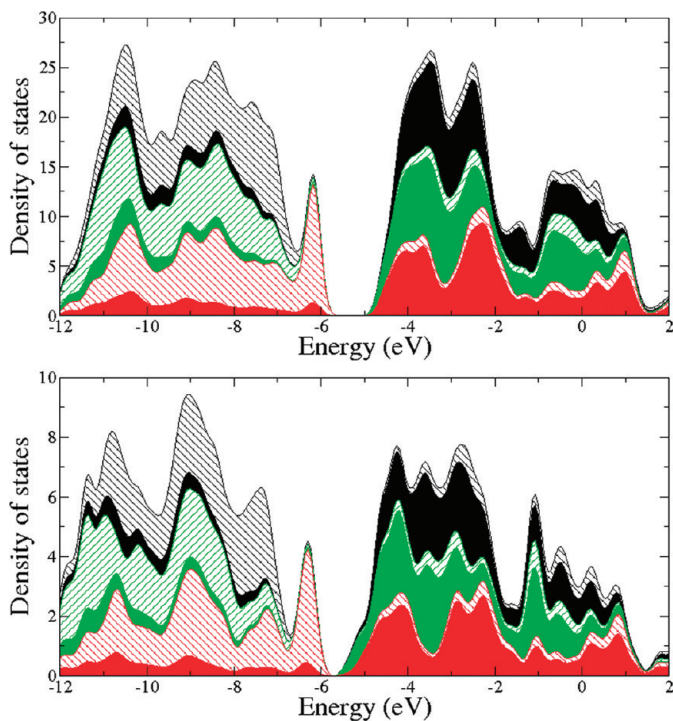


Figure 14. Contributions of Ti and O atoms layer by layer to the total DOS of three-layer rutile slabs (PBE results). Top panels: slabs with adsorbate. Bottom panels: slabs without adsorbate. Left column: constrained slabs. Right column: free slabs. Slabs without adsorbate display a shoulder peak near the CBM, which disappears when the benzoic acid molecule is adsorbed.

According to both PBE and B3LYP calculations, in slabs with adsorbates, the bottom of the conduction band (CB) is formed by a mixture of states on both subsurface and surface Ti atoms, especially those not taking part in bonding with the carboxylate. Unlike bare slabs, the DOS of odd- and even-layered rutile slabs with adsorbate are qualitatively quite similar to each other; the most noticeable difference is that states on Ti atoms bonded to the carboxylate appear at the CBM in even-layered slabs and slightly deeper in the CB in odd-layered slabs.

Similar to anatase calculations, the benzoic acid HOMO appears ~ 0.3 eV above the valence band edge of the unconstrained two-layer rutile slab in B3LYP calculations (or at the same energies as the CBM in PBE calculations of even-layered slabs), but slightly below the CBM in odd-layered slabs, both according to B3LYP and PBE. This again underscores the difference in the behavior of the even- and odd-layered slabs.

In both anatase (101) and rutile (110) slabs, constrained slabs have a smaller band gap than free slabs (the difference of 0.5–0.6 eV for all slab sizes considered here) because the top of the valence band in constrained slabs is formed mainly by states on fixed O atoms. However, the composition of the bottom of the conduction band is similar in constrained and free slabs.

On the basis of the DOS of rutile slabs, we suggest that even-layered slabs are more reliable for modeling rutile (110) surfaces and adsorption on these surfaces. As adsorption energies and band gaps are clearly not converged in slabs with two to five layers, the four-layer slabs seem a better model of this surface than two-layer slabs. This also means that modeling adsorption on rutile requires a much larger computational effort than adsorption on anatase.

4. Discussion and Conclusions

We modeled the geometry and electronic structure of rutile (110) and anatase (101) surfaces and adsorption of benzoic acid, a common bridging group in DSSC chromophores, on these surfaces. One of the aims of this paper was to compare the

description of these systems given by different DFT methods, keeping the same density functional (GGA PBE). Localized or plane-wave basis sets and all-electron or pseudopotential treatment were considered, using CRYSTAL06, SIESTA, and Quantum ESPRESSO packages. We find very good qualitative agreement and fairly good quantitative agreement between geometries, band gaps, and surface energies obtained using different methods. Noticeably, however, the plane-wave-based Quantum ESPRESSO calculations of slabs took up to 5–10 times as much time as localized basis set calculations of the same systems, although the computational times improved with the use of more processors. Taking into account the accuracy of the results and the computational cost of the calculations, we conclude that expensive plane-wave treatment can be avoided for TiO₂ (or used for few benchmark calculations), as the less expensive localized basis set treatment (CRYSTAL06 or SIESTA) appears to be equally accurate.

Using these techniques, we analyzed the density of states of rutile (110) and anatase (101) surfaces. Our calculations show that conduction band edge states are localized away from the surface of the slabs; however, as the density of states increases to an appreciable number, the local density of states becomes increasingly evenly spread throughout the cell. The valence band edge is a mixture of the bulk and surface states; it is dominated by the fixed atoms' states in constrained slabs.

We compared the GGA PBE electronic structures with those obtained using the hybrid B3LYP functional. As expected, the B3LYP band gaps are larger and closer to experimental values (although overestimated), but the composition of the valence and conduction bands is very similar when modeled with both PBE and B3LYP. This suggests that, if we are interested in a qualitative description of the electronic states, rather than in accurate values of band gaps, PBE can be used in place of the expensive B3LYP calculations.

The second aim of this study was to determine the effect of benzoic acid adsorption on the TiO₂ density of states. We find that adsorption of benzoic acid has little effect on the electronic structure of anatase (101) slabs, when the molecule is adsorbed both in the dissociated form and in the more stable nondissociated molecular form. The effect of the adsorbate on the density of states of rutile (110) slabs is more pronounced. Specifically, adsorption of benzoic acid increases the band gap of odd-layered rutile (110) slabs by raising the energies of subsurface Ti atoms states and thus raising the CBM. This effect is much stronger in odd- than in even-layered slabs and decreases as the slab thickness increases, suggesting that slabs for modeling the rutile (110) surface should have at least four layers. It is likely that the same effect on the electronic structure of rutile slabs will be caused by other molecular adsorbates as well. The main difference in the B3LYP and PBE descriptions of TiO₂ with adsorbed benzoic acid is that the benzoic acid HOMO appears slightly above the valence band edge in B3LYP (whereas it is at or below the valence band edge in PBE); however, this does not cause localization of TiO₂ electronic states and does not change the structure of the bands.

An accurate description of the electronic structure of substrate–adsorbate systems is essential for modeling electron-transfer processes at interfaces. For example, the rate of electron injection in DSSCs can be computed using⁷¹

$$\Gamma_{mn}(E) = \frac{2\pi}{\hbar} \sum_{kk'} V_{mk} V_{nk'}^* \rho_{kk'}(E) \quad (2)$$

The three terms in this equation that determine the injection rates are the couplings, V_{mk} , between localized atomic orbitals on the adsorbed molecule (indices m and n refer to the states on the molecule) and delocalized orbitals on the semiconductor (states k , k'), the energy-dependent local density of states in the conduction band of the semiconductor, $\rho_{kk'}(E)$ (i.e., the empty states available to accept the electrons), and the injection energy E_s . This equation shows that the rate of electron injection is directly proportional to the partial density of states on the semiconductor surface atoms—the $\rho_{kk'}(E)$ term. The coupling matrix elements V_{mk} quantify the interaction between the surface and the adsorbed chromophore. As this interaction is much greater for the surface layer of the slab than for any subsurface layers, the necessary requirement for efficient electron injection is a high density of states on the surface atoms, at the energy E equal to the electron injection energy. Factors that affect the surface atoms' density of states, such as the interaction with adsorbate, are, therefore, important for an accurate description of the electron injection process.

Finally, we comment on the limitations of DFT in describing the electronic structure of materials. It is known that DFT underestimates band gaps. It has been shown earlier^{33–35} and confirmed in this work that rutile and anatase band gaps are underestimated by ~1 eV with GGA, whereas B3LYP band gaps are more accurate (although still overestimated by 0.5–0.7 eV). This raises the question of applicability of GGA to the calculations of electron injection. However, we can assume that the LUMO of chromophore molecules will be underestimated by roughly the same amount as the CBM of TiO₂, and the cancellation of errors will make comparison of chromophore LUMOs and TiO₂ CB reasonable. The second problem of GGA is its tendency to delocalize electrons,³⁰ which makes GGA not applicable for systems with localized electronic states. In our case, however, TiO₂ slabs, both clean and with adsorbates, do not have any localized states, and we believe that the GGA description of the density of states is valid. The composition of the conduction band (which is most important for electron-transfer processes) is very similar in both our PBE and our B3LYP calculations. Although GGA will not be able to describe correctly the system after electron injection (with an excess electron possibly localized in the slab), we believe that it gives a qualitatively correct description of the states in the conduction band of TiO₂, which are available for electron injection. Note that, to describe the system *after* injection, more sophisticated methods are needed, for example, hybrid functionals or the DFT + U method. However, this is beyond the scope of this study.

In summary, we showed that different DFT methods are very consistent in their description of the electronic structure of TiO₂ slabs. The simulations of the density of states of TiO₂ slabs provide an important step in modeling electron-transfer processes. We showed that molecular adsorbates affect the density of states on the rutile (110) surface, although the effect on the anatase (101) surface is very weak. Equipped with the accurate description of the density of states of the TiO₂–adsorbate systems, we will be able to model electron-transfer processes in these systems, such as electron injection and recombination in DSSCs.

Acknowledgment. The authors acknowledge financial support from EPSRC (D.R.J. and A.T.) and ERC (N.M. and A.T.).

References and Notes

- (1) Mills, A.; Davies, R. H.; Worsley, D. *Chem. Soc. Rev.* **1993**, 22, 417–425.

- (2) O' Regan, B.; Grätzel, M. *Nature* **1991**, *353*, 737–740.
 (3) Weckhuysen, B. M.; Keller, D. E. *Catal. Today* **2002**, *78*, 25–46.
 (4) Liu, G.; Wang, L. Z.; Yang, H. G.; Cheng, H. M.; Lu, G. Q. *J. Mater. Chem.* **2010**, *20*, 831–843.
 (5) Linsebigler, A. L.; Lu, G. Q.; Yates, J. T. *Chem. Rev.* **1995**, *95*, 735–758.
 (6) Bozzi, A.; Yuranova, T.; Kiwi, J. *J. Photochem. Photobiol., A* **2005**, *172*, 27–34.
 (7) McCullagh, C.; Robertson, J. M. C.; Bahnemann, D. W.; Robertson, P. K. *J. Res. Chem. Intermed.* **2007**, *33*, 359–375.
 (8) Wendt, S.; Schaub, R.; Matthiesen, J.; Vestergaard, E. K.; Wahlstrom, E.; Rasmussen, M. D.; Thostorp, P.; Molina, L. M.; Laegsgaard, E.; Stensgaard, I.; Hammer, B.; Besenbacher, F. *Surf. Sci.* **2005**, *598*, 226–245.
 (9) Papageorgiou, A. C.; Beglitis, N. S.; Pang, C. L.; Teobaldi, G.; Cabailh, G.; Chen, Q.; Fisher, A.; Hofer, W. A.; Thornton, G. *Proc. Natl. Acad. Sci. U.S.A.* **2010**, *107*, 2391–2396.
 (10) Di Valentin, C.; Pacchioni, G.; Onishi, H.; Kudo, A. *Chem. Phys. Lett.* **2009**, *469*, 166–171.
 (11) Sambrano, J. R.; Nobrega, G. F.; Taft, C. A.; Andres, J.; Beltran, A. *Surf. Sci.* **2005**, *580*, 71–79.
 (12) Di Valentin, C.; Finazzi, E.; Pacchioni, G.; Selloni, A.; Livraghi, S.; Paganini, M. C.; Giannello, E. *Chem. Phys.* **2007**, *339*, 44–56.
 (13) Di Valentin, C.; Pacchioni, G.; Selloni, A. *Chem. Mater.* **2005**, *17*, 6656–6665.
 (14) Bates, S. P.; Kresse, G.; Gillan, M. J. *Surf. Sci.* **1998**, *409*, 336–349.
 (15) Vittadini, A.; Casarin, M.; Selloni, A. *Theor. Chem. Acc.* **2007**, *117*, 663–671.
 (16) Wang, Y.; Hwang, G. S. *Surf. Sci.* **2003**, *542*, 72–80.
 (17) Bredow, T. *Int. J. Quantum Chem.* **1999**, *75*, 127–132.
 (18) Diebold, U. *Surf. Sci. Rep.* **2003**, *48*, 53–229.
 (19) Anderson, N. A.; Lian, T. *Coord. Chem. Rev.* **2004**, *248*, 1231–1246.
 (20) Vittadini, A.; Selloni, A.; Rotzinger, F. P.; Gratzel, M. *J. Phys. Chem. B* **2000**, *104*, 1300–1306.
 (21) Persson, P.; Bergstrom, R.; Lunell, S. *J. Phys. Chem. B* **2000**, *104*, 10348–10351.
 (22) Kieu, L.; Boyd, P.; Idriss, H. *J. Mol. Catal. A: Chem.* **2001**, *176*, 117–125.
 (23) Ojamae, L.; Aulin, C.; Pedersen, H.; Kall, P. O. *J. Colloid Interface Sci.* **2006**, *296*, 71–78.
 (24) Mendive, C. B.; Bredow, T.; Feldhoff, A.; Blesa, M.; Bahnemann, D. *Phys. Chem. Chem. Phys.* **2008**, *10*, 1960–1974.
 (25) Nilsing, M.; Lunell, S.; Persson, P.; Ojamae, L. *Surf. Sci.* **2005**, *582*, 49–60.
 (26) Luschtinetz, R.; Frenzel, J.; Milek, T.; Seifert, G. *J. Phys. Chem. C* **2009**, *113*, 5730–5740.
 (27) Rego, L. G. C.; Batista, V. S. *J. Am. Chem. Soc.* **2003**, *125*, 7989–7997.
 (28) Xu, Y.; Chen, W.-K.; Liu, S.-H.; Cao, M.-J.; Li, J.-Q. *Chem. Phys.* **2007**, *331*, 275–282.
 (29) Terranova, U.; Bowler, D. R. *J. Phys. Chem. C* **2010**, *114*, 6491–6495.
 (30) Di Valentin, C.; Pacchioni, G.; Selloni, A. *Phys. Rev. B* **2006**, *97*, 166803.
 (31) Becke, A. D. *J. Chem. Phys.* **1993**, *98*, 5648–5652.
 (32) Adamo, C.; Barone, V. *J. Chem. Phys.* **1999**, *110*, 6158–6170.
 (33) Labat, F.; Baranek, P.; Domain, C.; Minot, C.; Adamo, C. *J. Chem. Phys.* **2007**, *126*, 154703.
 (34) Zhang, Y. F.; Lin, W.; Li, Y.; Ding, K. N.; Li, J. Q. *J. Phys. Chem. B* **2005**, *109*, 19270–19277.
 (35) Pacchioni, G. *J. Chem. Phys.* **2008**, *128*, 182505.
 (36) Lin, Z.; Orlov, A.; Lambert, R. M.; Payne, M. C. *J. Phys. Chem. B* **2005**, *109*, 20948–20952.
 (37) Morgan, B. J.; Watson, G. W. *Surf. Sci.* **2007**, *601*, 5034–5041.
 (38) Calzado, C. J.; Hernandez, N. C.; Sanz, J. F. *Phys. Rev. B* **2008**, *77*, 045118.
 (39) Mattioli, G.; Filippone, F.; Alippi, P.; Amore Bonapasta, A. *Phys. Rev. B* **2008**, *78*, 241201.
 (40) Morgan, B. J.; Watson, G. W. *J. Phys. Chem. C* **2009**, *113*, 7322–7328.
 (41) Payne, M. C.; Teter, M. P.; Allan, D. C.; Arias, T. A.; Joannopoulos, J. D. *Rev. Mod. Phys.* **1992**, *64*, 1045–1097.
 (42) Kresse, G.; Furthmüller, J. *Phys. Rev. B* **1996**, *54*, 11169–11186.
 (43) Segall, M. D.; Lindan, P. J. D.; Probert, M. J.; Pickard, C. J.; Hasnip, P. J.; Clark, S. J.; Payne, M. C. *J. Phys.: Condens. Matter* **2002**, *14*, 2717–2744.
 (44) Giannozzi, P.; et al. *J. Phys.: Condens. Matter* **2009**, *21*, 395502.
 (45) Dovesi, R.; Saunders, V. R.; Roetti, C.; Orlando, R.; Zicovich-Wilson, M.; Fascale, F.; Civalleri, B.; Doll, K.; Harrison, N. M.; Bush, I. J.; D'Arco, P.; Lunell, M. *CRYSTAL06 User's Manual*; University of Torino: Torino, Italy, 2006.
 (46) Soler, J. M.; Artacho, E.; Gale, J. D.; Garcia, A.; Junquera, J.; Ordejon, P.; Sanchez-Portal, D. *J. Phys.: Condens. Matter* **2002**, *14*, 2745–2779.
 (47) Baroni, S.; Dal Corso, A.; de Gironcoli, S.; Giannozzi, P. <http://www.pwscf.org>.
 (48) Perdew, J. P.; Burke, K.; Ernzerhof, M. *Phys. Rev. Lett.* **1996**, *77*, 3865–3868.
 (49) Vosko, S. H.; Wilk, L.; Nusair, M. *Can. J. Phys.* **1980**, *58*, 1200–1211.
 (50) Perdew, J. P.; Chevary, J. A.; Vosko, S. H.; Jackson, K. A.; Pederson, M. R.; Singh, D. J.; Fiolhais, C. *Phys. Rev. B* **1992**, *46*, 6671–6687.
 (51) Cora, F. *Mol. Phys.* **2005**, *103*, 2483–2496.
 (52) http://www.crystal.unito.it/Basis_Sets/Ptable.html.
 (53) Anderson, D. G. *JACM* **1965**, *12*, 547–560.
 (54) Hamann, D. R. *Phys. Rev. Lett.* **1979**, *42*, 662–665.
 (55) Labat, F.; Baranek, P.; Adamo, C. *J. Chem. Theory Comput.* **2008**, *4*, 341–352.
 (56) Boys, S.; Bernardi, F. *Mol. Phys.* **1970**, *19*, 553.
 (57) Wu, Z.; Cohen, R. E. *Phys. Rev. B* **2006**, *73*, 235116.
 (58) <http://www.icmab.es/siesta/>.
 (59) Junquera, J.; Zimmer, M.; Ordejon, P.; Ghosez, P. *Phys. Rev. B* **2003**, *67*, 155327.
 (60) Vanderbilt, D. *Phys. Rev. B* **1990**, *41*, 7892–7895.
 (61) Goniakowski, J.; Holender, J. M.; Kantorovich, L. N.; Gillan, M. J.; White, J. A. *Phys. Rev. B* **1996**, *57*, 957–960.
 (62) Lazzeri, M.; Vittadini, A.; Selloni, A. *Phys. Rev. B* **2001**, *63*, 155409.
 (63) Muscat, J.; Swamy, V.; Harrison, N. M. *Phys. Rev. B* **2002**, *65*, 224112.
 (64) Burdett, J. K.; Hughbanks, T.; Miller, G. J.; Richardson, J. W.; Smith, J. V. *J. Am. Chem. Soc.* **1987**, *109*, 3639–3646.
 (65) Cronemeyer, D. C. *Phys. Rev.* **1952**, *87*, 876–886.
 (66) Bredow, T.; Giordano, L.; Cinquini, F.; Pacchioni, G. *Phys. Rev. B* **2004**, *70*, 035419.
 (67) Bates, S. P.; Kresse, G.; Gillan, M. J. *Surf. Sci.* **1997**, *385*, 386–394.
 (68) von Oertzen, G. U.; Gerson, A. R. *Int. J. Quantum Chem.* **2006**, *106*, 2054–2064.
 (69) Chen, Q.; Tang, C.; Zheng, G. *Physica B* **2009**, *404*, 1074–1078.
 (70) Ramamoorthy, M.; Vanderbilt, D.; King-Smith, R. D. *Phys. Rev. B* **1994**, *49*, 16721–16727.
 (71) Jones, D. R.; Troisi, A. *Phys. Chem. Chem. Phys.* **2010**, *12*, 4625–4634.